International Core Journal of Engineering Volume 12 Issue 5, 2026
ISSN: 2414-1895 DOI: 10.6919/ICJE.202605_12(5).0017

Preparation of Co-BDC/$Ti_3C_2T_x$ Composite Materials for High-performance Supercapacitor Electrodes

Feng Cui[1], Jiangzhi Zi[2], and Xi Chen[2,*]

[1] School of Materials and Chemistry, University of Shanghai for Science and Technology, Shanghai 200093, China

[2] School of Artificial Intelligence Sciences and Technology, University of Shanghai for Science and Technology, Shanghai 200093, China

[*]Corresponding author Email: xichen@usst.edu.cn

Abstract

$Ti_3C_2T_x$ MXene holds great potential for supercapacitor electrodes, yet its performance is hindered by nanosheet restacking. Herein, a Co-BDC/$Ti_3C_2T_x$ composite is fabricated by in situ growth of a cobalt-based MOF on MXene nanosheets. This unique architecture synergistically integrates the high conductivity of MXene with the large surface area and rich pseudocapacitance of MOF, leading to significantly enhanced electrochemical performance. The composite electrode exhibits a superior areal capacitance of 10.31 F cm^{-2} at 2 mA cm^{-2}. A solid-state asymmetric supercapacitor constructed with this composite delivers an energy density of 0.741 mW cm^{-2} at a power density of 0.483 mWh cm^{-2} and retains 89% of its initial capacitance after 5000 cycles, highlighting its remarkable cycling stability. This work presents an effective strategy for designing high-performance MXene-based electrodes for next-generation flexible energy storage devices.

Keywords

Supercapacitor; Electrochemistry; Composite Materials; Energy Storage.

1. Introduction

The growing demand for renewable energy integration and the rapid evolution of flexible, portable electronics have intensified the need for advanced energy storage systems that deliver high energy density, high power density, and long-term cycling stability[1-2]. Supercapacitors, recognized for their exceptional power density, fast charge/discharge kinetics, and robust cycle life, are pivotal in this landscape[3].However, their relatively low energy density remains a critical bottleneck for wider application. The performance of supercapacitors is fundamentally governed by their electrode materials, making the design of electrodes with high specific capacity and excellent rate capability a primary research focus[4-6].

Metal-organic frameworks (MOFs) and two-dimensional transition metal carbides/nitrides (MXenes) represent two prominent classes of electrode materials, each with distinct advantages and limitations. MOFs possess ultrahigh surface area, tunable porosity, and rich redox-active sites, making them ideal for pseudocapacitive storage.Yet,their poor electrical conductivity often compromises rate performance[7]. MXenes, conversely, exhibit metallic conductivity, hydrophilicity, and mechanical strength, but their practical capacity is hampered by nanosheet restacking, which reduces accessible surface area and hinders ion diffusion[8-9].

Constructing hybrid composites of MOFs and MXenes presents a strategic avenue to synergistically overcome these individual shortcomings. In such architectures, the conductive MXene network can

ISSN: 2414-1895 DOI: 10.6919/ICJE.202605_12(5).0017

serve as a high-speed electron highway, mitigating the conductivity issue of MOFs. Simultaneously, the in-situ growth of MOFs on MXene sheets can act as effective spacers, preventing MXene restacking and exposing more active surfaces[10-11]. This complementary interaction facilitates efficient ion and electron transport, thereby enhancing both capacitive performance and structural stability. This study focuses on the design and fabrication of a novel Co-based MOF/MXene composite electrode[12]. Through systematic characterization and electrochemical analysis, we elucidate the correlation between its microstructure and its superior energy storage properties. The findings offer valuable insights for developing high-performance electrode materials for next-generation supercapacitors[13].

2. Experimental Section

2.1 Materials

All chemicals were of analytical grade and used as received. Titanium aluminum carbide (Ti_3AlC_2, 98%) powder and activated carbon (AC) were purchased from Titan Scientific Co., Ltd. (China). Cobalt nitrate hexahydrate ($Co(NO_3)_2 \cdot 6H_2O$, ≥99%) and terephthalic acid (BDC, ≥99%) were obtained from Aladdin Reagent Co., Ltd. (China). Lithium fluoride (LiF, ≥99%), hydrochloric acid (HCl, 36–38%), N,N-dimethylformamide (DMF, ≥99.5%), ethanol (C_2H_5OH, ≥99.7%), polyvinylpyrrolidone (PVP), potassium hydroxide (KOH, ≥95%), and polyvinyl alcohol (PVA) were supplied by Sinopharm Chemical Reagent Co., Ltd. (China). Deionized water (resistivity >18.2 MΩ·cm) was used throughout the experiments. Nickel foam (thickness 1.6 mm) was provided by Suzhou Sinero Technology Co., Ltd. (China).

2.2 Synthesis of $Ti_3C_2T_x$ MXene

$Ti_3C_2T_x$ powder was prepared from a Ti_3AlC_2 precursor via a mild etching method. First, 30 mL of 9 mol L^{-1} HCl was placed in a PTFE beaker, and 2.5 g of LiF was added. The solution was heated to 40 °C under continuous stirring. Subsequently, 1.5 g of Ti_3AlC_2 powder was added gradually in small portions. The reaction was maintained at 45 °C for 48 h. The product was transferred to centrifuge tubes and washed repeatedly via centrifugation. The precipitate was washed twice with 2 mol L^{-1} HCl, followed by repeated rinsing with deionized water and centrifugation until the pH of the supernatant reached ≥6. Finally, the product was freeze-dried under vacuum to obtain $Ti_3C_2T_x$ powder.

2.3 Synthesis of Co-BDC on Ni foam

Co-BDC was directly grown on Ni foam (NF) via a hydrothermal method. A solution of 200 mg $Co(NO_3)_2 \cdot 6H_2O$ in 15 mL deionized water was prepared. Separately, 15 mL DMF and 15 mL anhydrous ethanol were mixed, followed by the addition of 75 mg H_2BDC. The two solutions were then combined, and 200 mg PVP was added with stirring. The mixture was maintained at 80 °C for 12 h. After cooling to room temperature, the obtained Co-BDC/NF was washed with deionized water and ethanol, and finally dried at 60 °C.

2.4 Synthesis Procedure of Co-BDC/ $Ti_3C_2T_x$ Composite

First, 0.02 g of $Ti_3C_2T_x$ MXene powder was uniformly dispersed in 20 mL of DMF by ultrasonication for 30 min. Then, 0.2 g of $Co(NO_3)_2 \cdot 6H_2O$ was added, and the mixture was further sonicated for 30 min to allow electrostatic adsorption of Co^{2+} ions onto MXene sheets. Meanwhile, 0.15 g of BDC ligand was dissolved in 15 mL of DMF. The BDC solution was poured into the MXene–Co^{2+} suspension under stirring. The mixture was transferred to a 100 mL Teflon-lined autoclave and heated at 180 °C for 6 h. After cooling, the product was collected by centrifugation, washed thoroughly with deionized water and ethanol, and dried at 60 °C. The synthesis route is schematically shown in Fig. 1.

ISSN: 2414-1895 DOI: 10.6919/ICJE.202605_12(5).0017

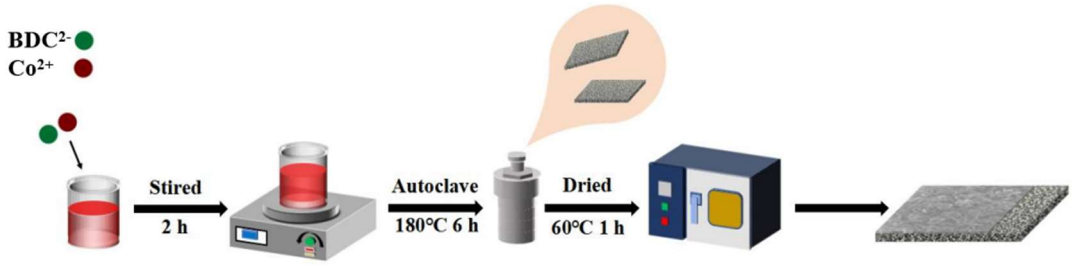

Fig. 1 Schematic illustration of the synthesis of the Co-BDC/$Ti_3C_2T_x$ composite

3. Results and Discussions

3.1 Structural Characterization of Materials

Single-layer $Ti_3C_2T_x$ was prepared from Ti_3AlC_2 powder via a mild etching method. Co-BDC was directly grown on nickel foam (NF) by a hydrothermal process. For the preparation of the Co-BDC/ $Ti_3C_2T_x$ composite, 30 mg of $Ti_3C_2T_x$ powder was added to the reaction system while keeping other reagents unchanged, resulting in the in-situ formation of the composite on the NF substrate.

Fig. 2a shows the X-ray diffraction (XRD) patterns of the prepared materials. A strong reflection peak at $2\theta = 8.07°$ is observed, which matches the single-crystal data of $Ti_3C_2T_x$, indicating the crystalline structure of the as-synthesized material. The XRD pattern of Co-BDC MOF coincides well with the simulated pattern of the MOF[14], confirming its successful synthesis. The XRD pattern of the $Ti_3C_2T_x$ /Co-BDC composite exhibits characteristic peaks corresponding to both Co-BDC and $Ti_3C_2T_x$, demonstrating the successful formation of the composite. Notably, the peak associated with the (002) plane of $Ti_3C_2T_x$ shifts from about 8° to 5.8°. This shift can be attributed to the intercalation of Co-BDC MOF into the interlayer space of $Ti_3C_2T_x$, which leads to an increase in the interlayer spacing. Moreover, the introduction of Co-BDC nanoparticles may reduce the crystallite size or introduce more structural defects in $Ti_3C_2T_x$, resulting in a higher degree of disorder. These structural changes are reflected in the decreased intensity and broadening of the $Ti_3C_2T_x$ diffraction peaks, indicating successful integration and modification of the $Ti_3C_2T_x$ structure within the composite.

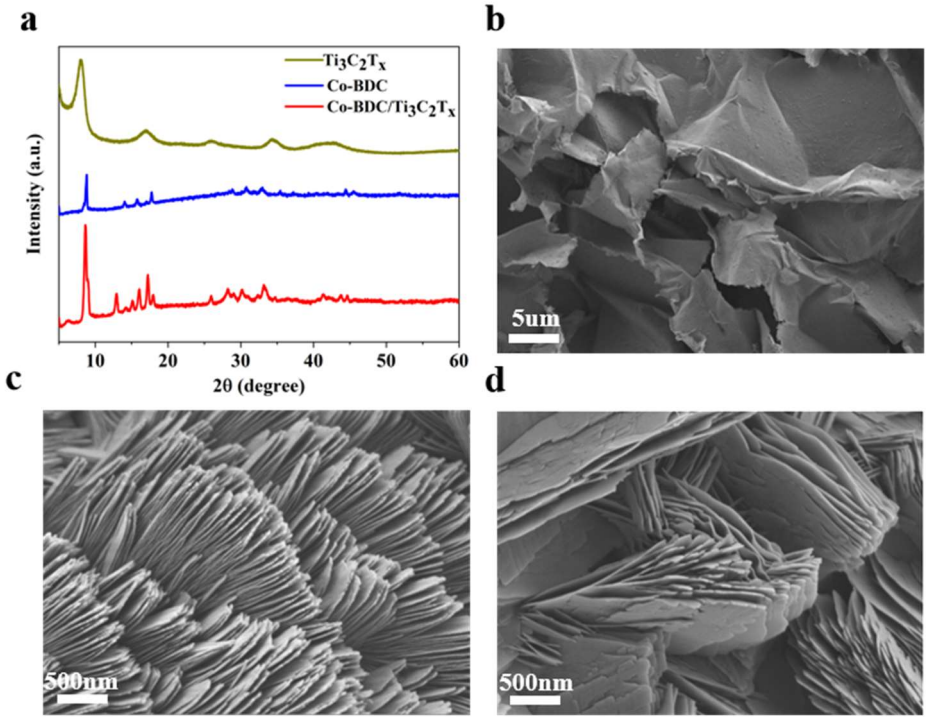

Fig. 2 (a) XRD patterns of $Ti_3C_2T_x$, Co-BDC, and Co-BDC/ $Ti_3C_2T_x$. (b) SEM image of $Ti_3C_2T_x$. (c) SEM image of Co-BDC. (d) SEM image of Co-BDC/ $Ti_3C_2T_x$ composite

ISSN: 2414-1895 DOI: 10.6919/ICJE.202605_12(5).0017

To elucidate the relationship between the surface morphology and electrochemical performance of the materials, scanning electron microscopy (SEM) was employed. Fig. 2b shows that the exfoliated MXene nanosheets predominantly consist of a few layers or even monolayers. Fig. 2c and 2d display the SEM images of Co-BDC and the Co-BDC/ $Ti_3C_2T_x$ composite, respectively. Both materials exhibit a sheet-like morphology, with the Co-BDC/ $Ti_3C_2T_x$ composite largely preserving the morphology of the MOF precursor, having an average sheet thickness of 20–25 nm.

Through electrostatic adsorption self-assembly followed by a solvothermal reaction, Co-BDC MOF was successfully intercalated into both the surface and interlayer spaces of $Ti_3C_2T_x$. The insertion of Co-BDC MOF nanoparticles led to an expansion of the interlayer spacing of MXene. While the transformation into composites or derivatives often risks damaging the original two-dimensional (2D) MOF morphology-which severely limits its practical application-the Co-BDC/$Ti_3C_2T_x$ nanocomposite prepared in this study remarkably retained the pristine sheet-like structure of its MOF precursor. This preserved 2D nanostructure confers two key advantages: (1) its large lateral dimensions endow it with excellent resistance to agglomeration during subsequent processing[15], and (2) its homogeneous local mechanical stress enables it to effectively accommodate volume changes during energy storage/conversion processes[16-17]. These characteristics collectively contribute to the outstanding electrochemical performance. Moreover, the enlarged interlayer spacing in $Ti_3C_2T_x$ likely provides a larger contact area for the electrolyte, promoting electrochemical reactions with the active sites in the material and further enhancing the overall electrochemical performance.

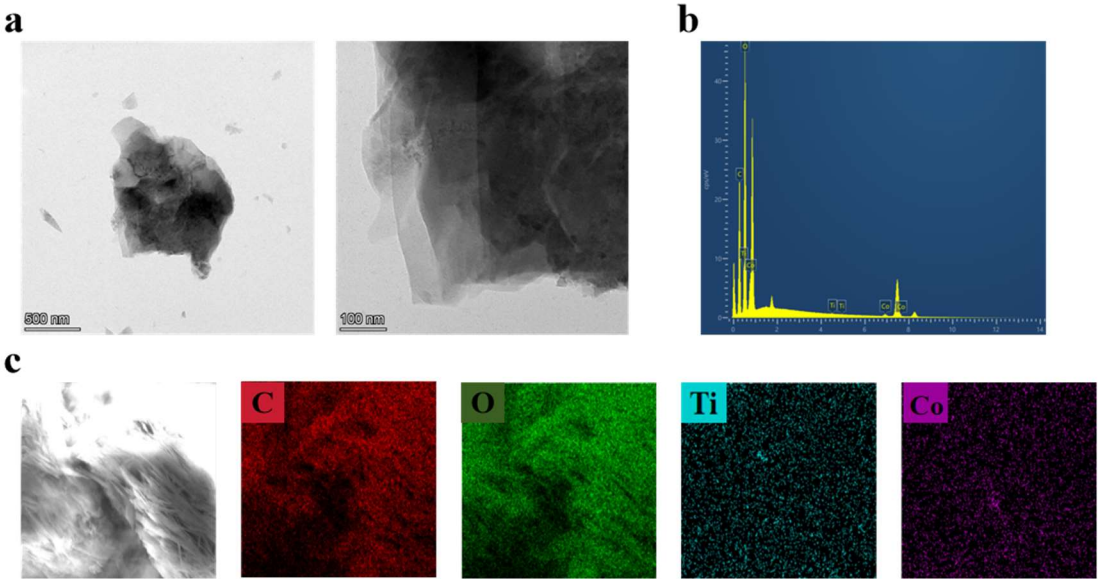

Fig. 3 (a) TEM image of the Co-BDC/$Ti_3C_2T_x$ composite. (b) EDS spectrum of the Co-BDC/$Ti_3C_2T_x$ composite. (c) Elemental mapping images showing the distribution of C, O, Ti, and Co in the Co-BDC/$Ti_3C_2T_x$ composite

The internal structure of the composite was further characterized by transmission electron microscopy (TEM). The TEM image in Fig. 3a clearly reveals the composite's microstructure. The material exhibits an irregular flaky morphology with distinct edges and characteristic wrinkles, consistent with the inherent two-dimensional layered structure of MXene ($Ti_3C_2T_x$). A large number of granular deposits, ranging in size from several tens to hundreds of nanometers, are uniformly distributed on the flake surfaces without significant agglomeration[18]. This provides direct visual evidence that Co-BDC MOF has been successfully loaded onto the $Ti_3C_2T_x$ surface, forming a heterojunction structure.The EDS spectrum in Fig. 3b further corroborates the chemical composition of the structure. Characteristic peaks for carbon (C) and titanium (Ti), originating from the $Ti_3C_2T_x$ substrate, are

ISSN: 2414-1895 DOI: 10.6919/ICJE.202605_12(5).0017

present. Moreover, distinct peaks for cobalt (Co) are observed at 0.77 keV and 6.93 keV, and an oxygen (O) peak is detected at 0.52 keV. The presence of these Co peaks directly confirms the successful incorporation of Co into the composite. The absence of signals from other impurity elements indicates a high-purity synthesis process. Fig. 3c shows the uniform distribution of C, O, Ti, and Co elements, demonstrating the successful formation of a well-integrated composite structure with Co-BDC MOF uniformly loaded on the $Ti_3C_2T_x$ MXene surface. The uniform loading observed at the nanoscale, combined with the elemental matching confirmed by EDS, jointly verifies the successful synthesis of the Co-BDC/ $Ti_3C_2T_x$ composite.

3.2 Performance of the Co-BDC/$Ti_3C_2T_x$ Electrode

A three-electrode test system was constructed using a platinum wire as the counter electrode, a saturated KCl-calomel electrode as the reference electrode, and Co-BDC/ $Ti_3C_2T_x$ (electrode area S = 1×1cm^2) as the working electrode. Electrochemical measurements were then performed on the Co-BDC/ $Ti_3C_2T_x$ composite.

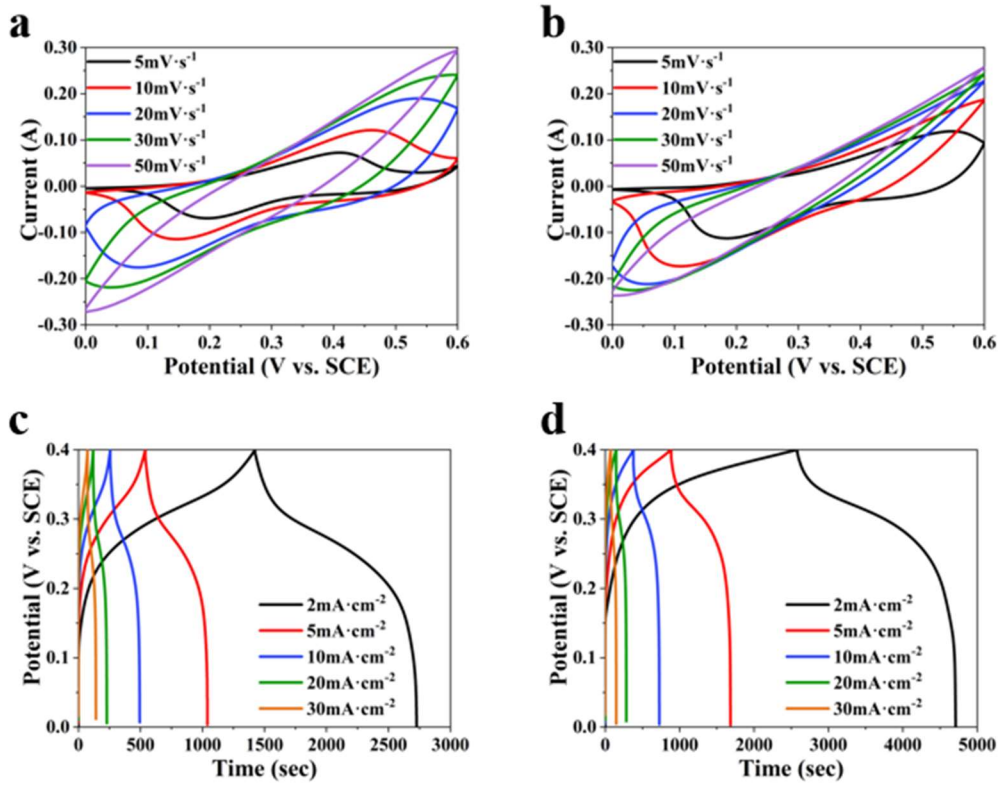

Fig. 4 Electrochemical performance of Co-BDC and Co-BDC/ $Ti_3C_2T_x$. (a) CV curves of Co-BDC. (b) CV curves of Co-BDC/ $Ti_3C_2T_x$. (c) GCD profiles of Co-BDC. (d) GCD profiles of Co-BDC/ $Ti_3C_2T_x$

Fig. 4 shows the cyclic voltammetry (CV) curves and galvanostatic charge-discharge (GCD) profiles of Co-BDC and Co-BDC/ $Ti_3C_2T_x$ at various scan rates (5 mV s^{-1} to 50 mV s^{-1}) and current densities, respectively. All CV curves exhibit a quasi-rectangular shape with distinct redox peaks, indicating pseudocapacitive behavior. Compared with the CV curve of pure Co-BDC (Fig. 4a), the Co-BDC/ $Ti_3C_2T_x$ composite (Fig. 4b) shows higher redox-peak currents and a larger enclosed area, suggesting enhanced capacitive performance. Figures 4c and 4d display the GCD voltage profiles measured at different current densities ranging from 2 mA cm^{-2} to 30 mA cm^{-2}. All GCD curves present well-defined charge-discharge plateaus, consistent with the CV results, confirming the pseudocapacitive nature of the composite. In comparison with the GCD curve of pure Co-BDC (Fig. 4c), the discharge time of Co-BDC/ $Ti_3C_2T_x$ (Fig. 4d) is significantly longer, further demonstrating

ISSN: 2414-1895 DOI: 10.6919/ICJE.202605_12(5).0017

the improved capacitance of the composite. The areal capacitance (C_s) was calculated using the formula:

$$C_s = \frac{I\Delta t}{\Delta v S} \tag{1}$$

The calculated areal capacitance of Co-BDC/ $Ti_3C_2T_x$ at 2 mA cm^{-2} is 10.31 F cm^{-2}, which is significantly higher than that of pure Co-BDC (6.23 F cm^{-2}). The superior specific capacitance of the Co-BDC/ $Ti_3C_2T_x$ composite can be attributed to the enlarged interlayer spacing induced by the incorporation of Co-BDC and the high electrical conductivity of $Ti_3C_2T_x$.

3.3 Supercapacitor Performance

An all-solid-state supercapacitor was assembled using activated carbon and a PVA/KOH gel electrolyte. Fig. 5a shows the CV curves of the Co-BDC/ $Ti_3C_2T_x$ supercapacitor at scan rates from 5 to 100 mV·s^{-1}. The CV profiles are quasi-rectangular with clear redox peaks, especially a pair of anodic/cathodic peaks between 0.4 and 0.8 V, confirming the pseudocapacitive nature of the device originating from the reversible Co^{2+}redox reactions in Co-BDC[19-20]. The increase in the CV integrated area with scan rate demonstrates good rate capability. Compared with ideal double-layer capacitance, the shape highlights the faradaic-reaction-dominated storage mechanism.Using equations (2) and (3) (shown below), the device delivers an energy density (E_s) of 0.483 mWh·cm^{-2} and a power density (P_s) of 0.741 mW·cm^{-2} at 2 mA cm^{-2}, indicating excellent energy-storage performance.

$$Es = \frac{I\int Vdt}{S} \tag{2}$$

$$Ps = \frac{Es}{\Delta t} \tag{3}$$

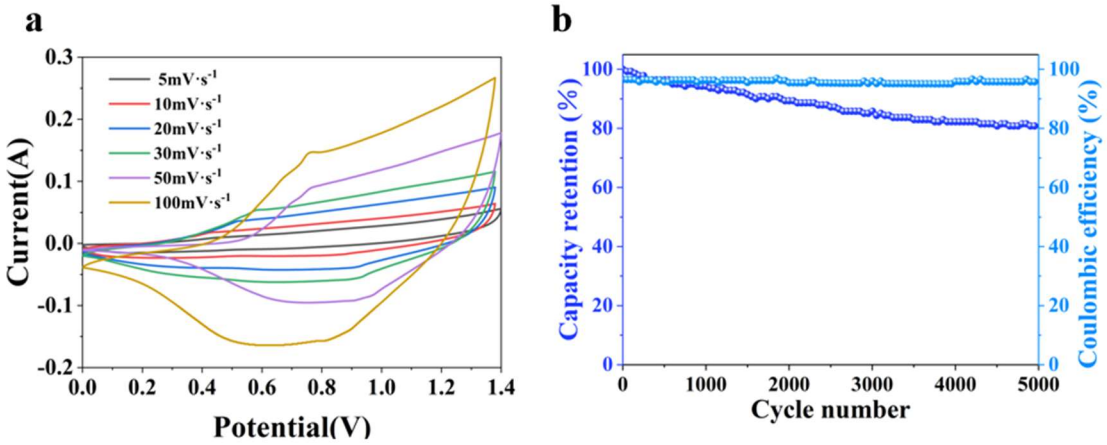

Fig. 5 Electrochemical performance of the Co-BDC/ $Ti_3C_2T_x$ supercapacitor.(a) Cyclic voltammetry (CV) curves of the supercapacitor at different scan rates. (b) Capacitance retention of the supercapacitor after 5000 charge–discharge cycles.

As shown in Fig. 5b, the long-term cycling stability was tested at 80 mA cm^{-2}. After 5000 continuous charge–discharge cycles, the capacitance retention remains about 89%, and the Coulombic efficiency

ISSN: 2414-1895 DOI: 10.6919/ICJE.202605_12(5).0017

stays close to 100%, indicating negligible capacity decay or side reactions. This excellent durability benefits from the synergy between the highly conductive $Ti_3C_2T_x$ MXene and the stable Co-BDC MOF skeleton, which effectively suppresses structural collapse and active-material detachment[20-21]. The stable capacitance retention and Coulombic efficiency further verify the reliability of the composite for high-energy-density, long-life supercapacitor applications.

4. Conclusion

In summary, a novel Co-BDC/ $Ti_3C_2T_x$ composite electrode was successfully fabricated through an in-situ growth strategy combining electrostatic self-assembly and solvothermal treatment. The composite retains the two-dimensional sheet-like morphology of the MOF precursor while effectively preventing the restacking of MXene layers. Structural and compositional characterizations confirm the uniform distribution of Co-BDC on the $Ti_3C_2T_x$ surface and the expansion of the MXene interlayer spacing, which together provide abundant electrochemically active sites and efficient pathways for ion/electron transport. When evaluated as a supercapacitor electrode, the composite exhibits significantly enhanced areal capacitance (10.31 $F \cdot cm^{-2}$ at 2 $mA \cdot cm^{-2}$) compared to pure Co-BDC (6.23 F cm^{-2}), along with good rate capability and cycling stability. The assembled solid-state asymmetric supercapacitor delivers a high energy density of 0.483 $mWh \cdot cm^{-2}$ at a power density of 0.741 $mW \cdot cm^{-2}$, and retains 89% of its initial capacitance after 5000 cycles, demonstrating excellent long-term durability. The improved performance is attributed to the synergistic effects between the conductive MXene network and the pseudocapacitive MOF, which facilitate charge storage and structural integrity. This work provides a feasible and effective approach for designing high-performance MXene-based composite electrodes, and offers valuable insights for developing flexible, high-energy-density energy-storage devices.

References

[1] Bommireddy P R, Chandra Sekhar M, Lee Y-W, et al. Binder-free Co–Ni hexacyanoferrate as a battery-type electrode material for hybrid supercapacitors [J]. Ceram Int, 2022, 48(8): 11849-11857.

[2] Lu J, Zhang J, Wang X, et al. A review of advanced electrolytes for supercapacitors [J]. Journal of Energy Storage, 2024, 103: 114338.

[3] Rachiy B I, Nykoliuk M O, Budzulyak I M, et al. Ultrasonic modification of carbon materials for electrochemical capacitors [J]. Nanoscale Research Letters, 2017, 12(1): 79.

[4] Lei Y, Ossonon B D, Chen J, et al. Electrochemical characterization of graphene-type materials obtained by electrochemical exfoliation of graphite [J]. J Electroanal Chem, 2021, 887: 115084.

[5] Li J, Tian L, Liang F, et al. Molten salt synthesis of hierarchical porous N-doped carbon submicrospheres for multifunctional applications: High performance supercapacitor, dye removal and CO2 capture [J]. Carbon, 2019, 141: 739-747.

[6] Gazigil L, Er E, Yonar T. Determination of the optimum conditions for electrochemical regeneration of exhausted activated carbon [J]. Diamond Relat Mater, 2023, 133: 109741.

[7] Mandal S, Mendhe A B, Rakhade H M, et al. Recent advancement and design in supercapacitor hybrid electrode materials: Bridging the gap between energy and power density [J]. Chemical Engineering Journal Advances, 2025, 21: 100690.

[8] Maria Mahimai B, Li E, Pang J, et al. Interface engineering in conducting polymers-based supercapacitor [J]. Journal of Energy Storage, 2024, 96: 112598.

[9] Fazal A, Zafar M M, Iqbal M J, et al. High-performance supercapacitor electrode synthesized by in-situ chemical oxidative polymerization of TiO2/PANI composite [J]. Synth Met, 2025, 311: 117842.

[10] Li G, Feng Y, Yang Y, et al. Recent advances in transition metal phosphide materials: Synthesis and applications in supercapacitors [J]. Nano Materials Science, 2024, 6(2): 174-192.

[11] Reenu, Sonia, Phor L, et al. Electrode materials for supercapacitors: A comprehensive review of advancements and performance [J]. Journal of Energy Storage, 2024, 84: 110698.

[12] Cao Z, Momen R, Tao S, et al. Metal–Organic Framework Materials for Electrochemical Supercapacitors [J]. Nano-Micro Lett, 2022, 14(1): 181.

ISSN: 2414-1895 DOI: 10.6919/ICJE.202605_12(5).0017

[13] Oh S, Lee S, Kim H, et al. Reduced graphene oxide composite fiber with hierarchical pores for all-solid-state fiber supercapacitors [J]. Carbon, 2025, 234: 119998.

[14] Sun X, Li Y, Su H, et al. Dissecting π-conjugated covalent-coupling over conductive MOFs toward efficient two-electron oxygen reduction [J]. Appl Catal B-Environ, 2022, 317: 121706.

[15] Saad A, Biswas S, Gkaniatsou E, et al. Metal–Organic Framework Based 1D Nanostructures and Their Superstructures: Synthesis, Microstructure, and Properties [J]. Chem Mater, 2021, 33(15): 5825-5849.

[16] Hang X, Xue Y, Cheng Y, et al. From Co-MOF to CoNi-MOF to Ni-MOF: A Facile Synthesis of 1D Micro-/Nanomaterials [J]. lnorg Chem, 2021, 60(17): 13168-13176.

[17] Snowlin V, Snowban J, Prabu H J, et al. Facile solvothermal fabrication of cobalt-metal–organic framework (Co-MOF)-based electrode material for supercapacitor devices [J]. Journal of Materials Science: Materials in Electronics, 2025, 36(24): 1512.

[18] Jones C W. Metal–Organic Frameworks and Covalent Organic Frameworks: Emerging Advances and Applications [J]. JACS Au, 2022, 2(7): 1504-1505.

[19] Bhoite A A, Tarwal N L. Metal-organic frameworks (MOFs) and their composites as electrode materials for supercapacitor applications [J]. Sustainable Materials and Technologies, 2026, 48: e01956.

[20] Liu Z, Wang L, Yuan G, et al. Recent advances of metal-organic frameworks/carbon composites for rechargeable batteries [J]. Coord Chem Rev, 2026, 556: 217661.

[21] Braga A L, Lima T A S, Fortunato V D S, et al. Co-BDC MOF/Graphene Nanohybrid as an Efficient Electrode Material for High-Performance Supercapacitors [J]. ACS Omega, 2026, 11(11): 17732-17745.